Study of $^{nat}B(^3He,p)$ reactions cross sections using a novel setup for ^{3}He-NRA micro analyses

Toni Dunatov[a], Georgios Provatas*[a], Stjepko Fazinić[a], Varvara Foteinou[b], Fotios Maragkos[b], Karla Ivanković Nizić[a], Maja Mičetić[a]

[a]*Ruđer Bošković Institute, Zagreb, Croatia*
[b]*RUBION, Zentrale Einrichtung für Ionenstrahlen und Radionuklide, Ruhr-Universität Bochum, Germany*

***corresponding author: georgios.provatas@irb.hr**

Abstract

In the present work experimentally determined differential cross sections of the reactions $^{10}B(^3He, p_{1,3})^{12}C$, $^{11}B(^3He, p_{0,1,2,3})^{13}C$ and $^{11}B(^3He, d_0)^{12}C$ are reported. The measurements cover the 2 - 3 MeV energy range, for 5 detection angles of θ = 137°, 141°, 146°, 152°, 158°. A novel experimental setup was designed for this purpose and installed at the Dual Microprobe end-station of the Ruđer Bošković Institute (RBI) in Zagreb, Croatia. It involves an annular strip charged particle silicon detector with a large solid angle, enabling a relatively fast acquisition process without significant increase in the angular uncertainty. The obtained cross sections were benchmarked with a thick amorphous boron target in a different experimental setup at RBI, as well as at the scattering chamber setup of the RUBION accelerator facility in Bochum, Germany.

Keywords: Nuclear reaction analysis; Ion beam analysis; helium-3; fusion materials

1 Introduction

In Ion beam analysis, (IBA) ions accelerated in the MeV energy range are used to examine the composition of samples, based on the knowledge of ion interactions with matter such as the nuclear reaction cross sections. Good knowledge of such cross sections is essential for obtaining accurate quantitative results when applying the Nuclear Reaction Analysis (NRA) technique.

In particular, ^{3}He-NRA has recently been shown to be useful for examining plasma facing components in experimental fusion reactors in combination with other material analysis techniques [1]. Most of the relevant light elements and isotopes can be probed using NRA, with deuterium being especially interesting in fusion applications as it is part of the fusion fuel. In parallel, PIXE (Particle Induced X-ray Emission Spectroscopy) can extract information on the heavier elements' concentrations. A focused ion microbeam can be scanned over a certain sample to also give spatial distributions of elements/isotopes. This allows for the analysis of microscopic samples, sometimes referred to as μNRA, which can be necessary depending on the application, For instance, this technique was demonstrated in several works, where the compositions of fusion dust particles were analyzed to investigate erosion of the plasma facing components and co-deposition with the fusion fuel [2].

There is, however, a significant lack of relevant fundamental parameters for these applications. Precise knowledge of the stopping power of ions in matter and nuclear reaction cross sections is needed. In particular, there is a lack of availability of cross section data for ^{3}He-induced reactions, mostly because of its high cost. Reliable measurements of these reactions at typical exit backward angles have therefore been identified as one of the high priority requirements for IBA applications in this field. Both the measurement of new reliable data and the re-examination of existing data is necessary. This has been recognized by the International Atomic Energy Agency by establishment of a Coordinated Research Project on the development and applications of Ion Beam Techniques for Materials irradiation and Characterization relevant to Fusion technology.

In the present work, ^{3}He-induced reaction differential cross sections on boron for the ^{10}B(^{3}He, $p_{1,3}$)^{12}C, ^{11}B(^{3}He,$p_{0,1,2,3}$)^{13}C and ^{11}B(^{3}He, d_0)^{12}C reaction channels were measured. In tokamaks, boronization of the inner walls is often used to improve oxygen gettering from the plasma and therefore reduce plasma impurities. Boron could therefore often be found as a component of the fusion dust eroded from the reactor walls. Recently, the design of the ITER reactor plasma facing components shifted from a combination of Be and W to only using W, and consequently boronization will be needed in ITER as well [3]. Therefore, to ensure good performance of ITER, further plasma campaigns and subsequent analyses are needed on current tokamaks. Understanding the boron erosion and co-deposition with deuterium and especially tritium is crucial, as tritium content is a potential issue in the performance of ITER.

The main focus of the measurements was on the higher Q-value reactions, as those are particularly useful for the NRA analysis of boron. However, the data from the lower energy channels is also important for the analysis of the whole energy range of the obtained NRA spectra. For instance, due to the Q-values of the reactions and the energy loss inside the analysis samples, there are potential overlaps between the NRA peaks corresponding to the D(^{3}He,p)^{4}He and ^{11}B(^{3}He,p_0)^{13}C or ^{10}B(^{3}He,p_1)^{12}C reactions. Furthermore, the data available in the literature for this energy range is limited to detection angles of 90°, 135° and 150°, and for the ^{11}B(^{3}He ,$p_{1,2,3}$)^{13}C reactions the individual peaks are not resolved and only the summed cross sections are available.

Previous measurements [4] [5] on Be and C cross sections, conducted with a Double Side Silicon Strip Detector (DSSSD) at the RBI charged particle spectroscopy chamber, obtained very detailed data, however at the cost of a complex data acquisition and a time consuming data analysis of 64 pulse height spectra for each beam energy. At the same time applications of μNRA, limiting the impinging beam currents below 1 nA, can suffer from similar issues, when using NRA setups equipped with typical SSB detectors.

Increasing the solid angle for μNRA applications as much as possible is needed for quantifying accurately the elements present in low concentrations. However, in some cases this increase in solid angle is obtained at the cost of a poorly-defined detection (backwards) angle, which also complicates the analysis [6]. Therefore, in the present work, a simpler measurement technique is introduced, intended to be used both for cross section measurements and μNRA applications. It involves a nanometer precision piezo stage for precise target positioning and an annular silicon detector with 5 concentric strips [7]. The latter can achieve a large solid angle (≈ 0.30 sr per strip) and an angular acceptance of approximately ± 2.5° per strip, depending on the distance. The setup was initially calibrated using well known resonant reactions to confirm the angular definition.

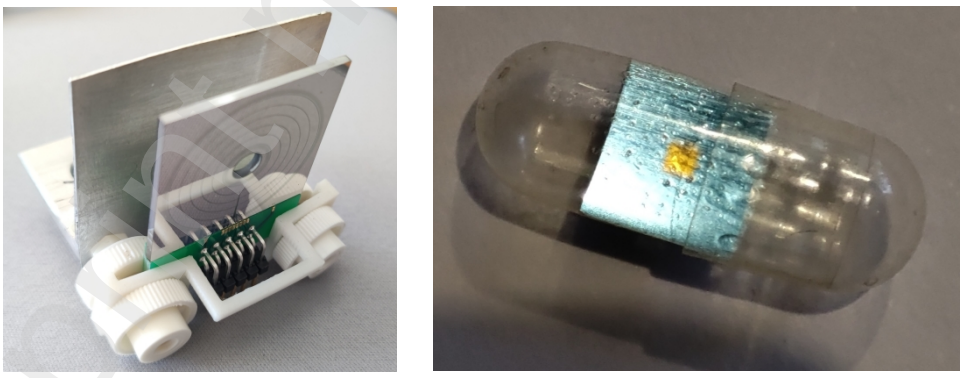

Figure 1: Image of the detector setup and the Si_3N_4 sample used

2 Experimental

2.1 Measurement Setup

The cross-section measurements were carried out at the RBI Tandem accelerator facility managed by the Laboratory for ion beam interactions in the Dual Microbeam (DuMi) end-station vacuum chamber [8] using ^{3}He ion beams from the 1 MV Tandetron accelerator.
The main part of the present setup is a 5-strip annular detector custom designed and obtained from Micron Semiconductors [7]. The detector was mounted in the chamber in the 3D printed holder. The sample holder is equipped with a precise XYZ motor, viewed with a CCD fine camera with 3 mm field attached to the microscope with a fixed working distance. Therefore, the positioning of the sample enables the precise definition of backward detection angles for measurement. For the experiment, the target to the detector plane distance was set at d = 13.90 mm. The setup can be easily modified to obtain a different set of backward detection angles by simply changing the distance d.

In order to check the performance of this novel setup, it was initially tested through the measurement of the well-studied ^{28}Si(p,p$_0$)^{28}Si elastic backscattering reaction on a 100 nm thin Si_3N_4 sample. This reaction exhibits a resonance at 1645 keV [9] with strong angular dependence allowing for simultaneous calibration of the ^{3}He ion beam energy from the accelerator and the angular definition of each of the detector's strips.

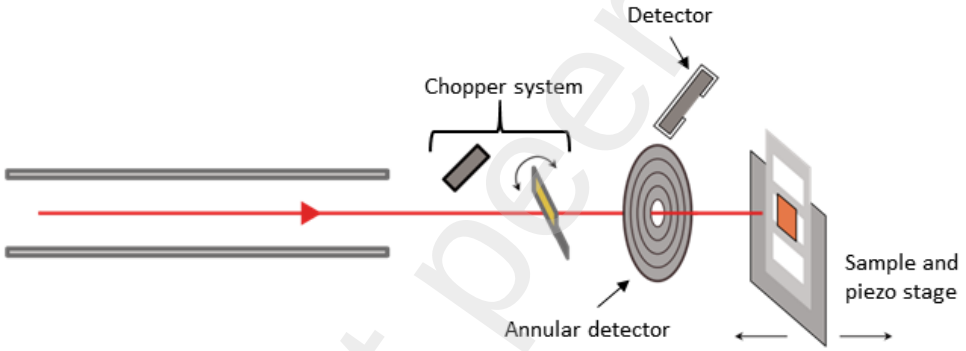

Figure 2 - Schematic of the experimental setup used.

2.2 Measurements

Thin boron films were deposited at RBI using the magnetron sputtering technique. The deposition was performed using CMS-18 K.J. Lesker magnetron sputtering deposition system. Sputtering power od B target was 130 W, using Ar as working gas under pressure of 3.5 mTorr. The deposition was performed in duration of 8 h, at room temperature.

A layer of gold was then evaporated on top for ion beam fluence normalization. The cross section was calculated relative to the known Rutherford elastic backscattering cross section of gold. With this method possible systematic uncertainties in the absolute determination of the accumulated charge and the detector solid angles are eliminated. Denoting the counts of boron and gold as I_B and I_{Au} the differential cross section is obtained as:

$$\frac{d\sigma_B}{d\Omega}(\theta, E) = \frac{I_B N_{Au}}{I_{Au} N_B f_I} \frac{d\sigma_{Au}}{d\Omega}(\theta, E) = \frac{\lambda}{f_I} \frac{I_B}{I_{Au}} \frac{d\sigma_{Au}}{d\Omega}(\theta, E). \quad (1)$$

Where f_I is the isotopic fraction of the isotope in question, i.e. 0.8 for ^{11}B and 0.2 for ^{10}B. This formula is used in calculating the cross section. Only the relative thickness of the layers defined as $\lambda = N_{Au}/N_B$ is therefore needed.

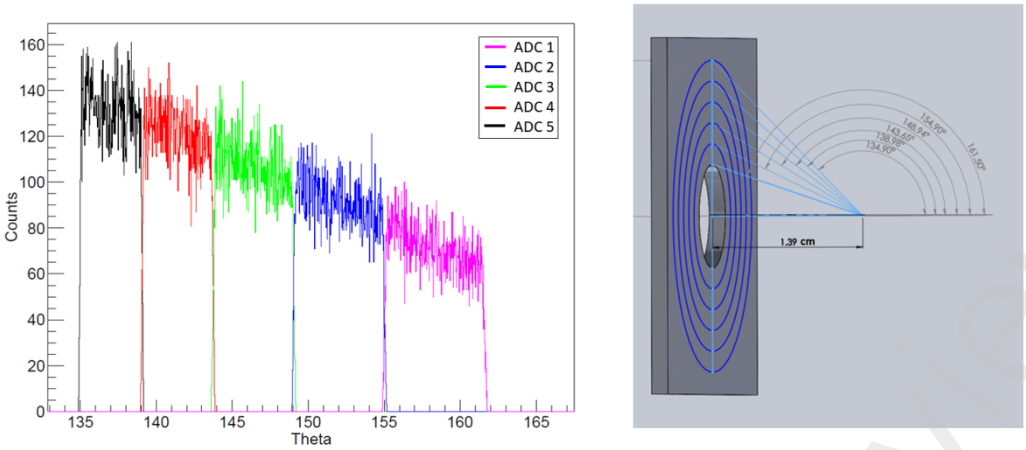

Figure 3 - Monte Carlo simulation and an analytical calculation of the geometrical angles

Boron was evaporated on the same Si_3N_4 target used in the angle calibration process, which was then used for the cross-section measurements. The cross-section measurements were conducted with a focused beam (≈ 10 µm) scanned over the target within the thin 1x1 mm^2 window. The NRA spectra were collected at energies from 2 to 3 MeV, starting with 3 MeV and then reducing in 100 keV steps down to 2 MeV, with a beam current of ~ 2.5 nA. Spectra were collected for approx. 2 hours per energy to obtain a minimum of 1000 counts per peak in the two highest energy peaks ($^{10}B(^3He, p_1)^{12}C$ and $^{11}B(^3He, p_0)^{13}C$).

To avoid possible systematic uncertainties additional data points were also collected using a different setup in the other RBI microprobe beamline [10], and another accelerator, the 6 MV Tandem Van de Graaff (VDG). A typical SBD charged particle detector was mounted at the 135° port of the vacuum chamber. Two data points, at 2.6 and 3 MeV, were measured with a millimeter-sized spot on the same target. Again, the cross sections were obtained relative to the Rutherford cross sections on gold, using the intensity of the RBS peak of gold from the target. In addition, the $Qx\Omega$ (total accumulated charge x detector solid angle) value was also obtained independently using the chopper system in front of the microprobe vacuum chamber.

The chopper setup consists of a detector mounted next to a graphite foil with a thin layer of gold on top. The foil is connected to a step motor and periodically intercepts the beam. A continuous measurement of the ion beam current is then provided by the integral of the RBS gold peak from the foil measured by the chopper detector. The calibration of the SBD detector solid angle was performed relative to a known $Qx\Omega$ value obtained by fitting the RBS spectrum from a thick reference Au target in SIMNRA [11].

2.3 Target characterization and benchmarking

The microprobe setup and the VDG accelerator were also used to determine the thickness of the ^{nat}B target. This was measured both with proton-EBS (Elastic Backscattering Spectrometry) and proton-NRA through the $^{11}B(p,\alpha)^8Be$ reaction by implementing a measurement with a 2.6 MeV proton beam. Both cross section values were taken from Kokkoris et al. on IBANDL [12]. In this energy range, the cross-section values used for the elastic scattering also agree with the ones by Chiari et al [13]. The Chiari et al. EBS data was used for determining the ^{10}B content. From these measurements the natural isotopic content of the target (20% ^{10}B and 80% ^{11}B) was confirmed within measurement error. Since the boron target has natural isotopic content, the weighted average of the ^{10}B and ^{11}B EBS and ^{11}B NRA measurements was taken and the resulting composition of the target is:

$$N_{natB} = (1000 \pm 30) \times 10^{15}\ at/cm^2$$

$$N_{Au} = (11.9 \pm 0.4) \times 10^{15}\ at/cm^2$$

$$\lambda = \frac{N_{Au}}{N_{natB}} = 0.0119 \pm 0.003$$

In addition to the thin target measurements, a benchmarking of the resulting cross sections was conducted using a ^{3}He beam and a thick compressed B target with an Au layer evaporated on top. The composition of this target was measured using proton EBS at 1.8 MeV. The obtained content of the target is 89.6 % B, 8.5% O 1.5% C and 0.4% Fe with a thickness of the evaporated gold layer of N_{Au}= 2.3 x 10^{15} at/cm^2.

The latter thick target benchmarking spectra were collected in the DuMi chamber using an ORTEC BA-022−300−2000 Partially Depleted Silicon Surface Barrier (PDSSB) detector mounted at 135° with an aperture restricting the diameter to 2 mm. Normalization was done based on the Rutherford backscattering from the gold layer and additionally on the chopper system. Moreover, thick target NRA spectra were also obtained independently at the experimental setup of RUBION Bochum [14] using the same thick compressed B target.

3 Results and discussion

Experimental spectra obtained for the detector angle calibration for one of the detector strips and for boron cross section measurement (for the same reaction angle) are shown in Figure 4 and Figure 6 with the corresponding peak identification. The measured cross sections of elastic scattering on Si, used for the detector's angles calibration, were determined using the same formula as the B cross section measurements (Equation 1). The intensities of the peaks were obtained by fitting of the spectra using the tv software [15]. The screened Rutherford cross section was calculated for the elastic scattering from gold, for each angle. The benchmarking spectra were simulated using SIMNRA 7.03 [11] .

The minimum and maximum angles of each detector strip, denoted here as θ_1 and θ_2 can be calculated analytically based on the geometry of the detector as $\theta = \arctan\frac{r}{d}$, where d = 13.9 mm is the fixed distance from the sample to the detector and r the distance from the center of the detector to the edge of a given strip. Integrating over θ we obtain the solid angle of a strip as:

$$\Omega = 2\pi\,(\cos\theta_2 - \cos\theta_1)$$

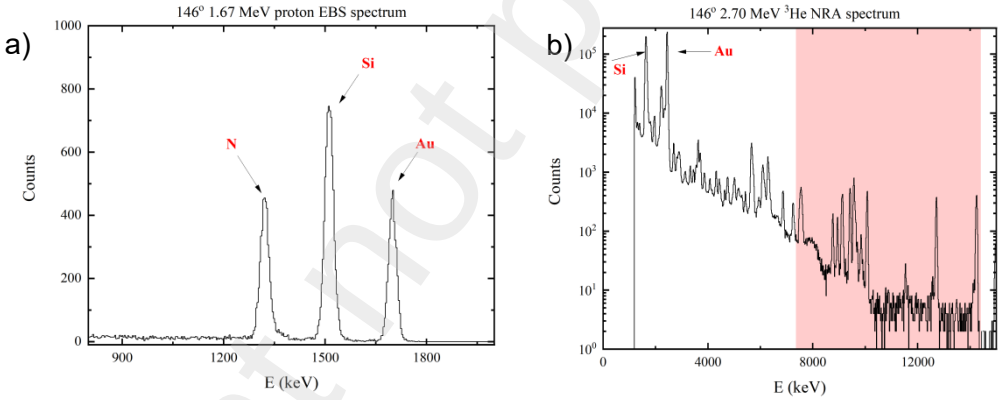

Figure 4 - Example spectra from a) reaction angle calibration using Si EBS, b) cross section measurement with ^{3}He. The boron peaks are in the higher energy area (shaded), shown in more detail in Figure 6

The detection angles reported with the data (158°, 152°, 146°, 141°and 137°) are the mean values over the solid angles covered by each detector strip defined so that $\sin\bar{\theta}(\theta_2 - \theta_1) = \int_{\theta_1}^{\theta_2}\sin\theta\ d\theta$. For small differences this is approximately the same as the arithmetic mean $\bar{\theta} = \frac{\theta_1 + \theta_2}{2}$. To confirm these values, the setup was also simulated using Geant4 with an isotropic source of 1 mm diameter. The counts obtained and the values of the solid angle calculation are shown in Figure 3. Results of the reaction angle calibration are also shown in Figure 5 with the values of θ_1 and θ_2 for the middle detector strip.

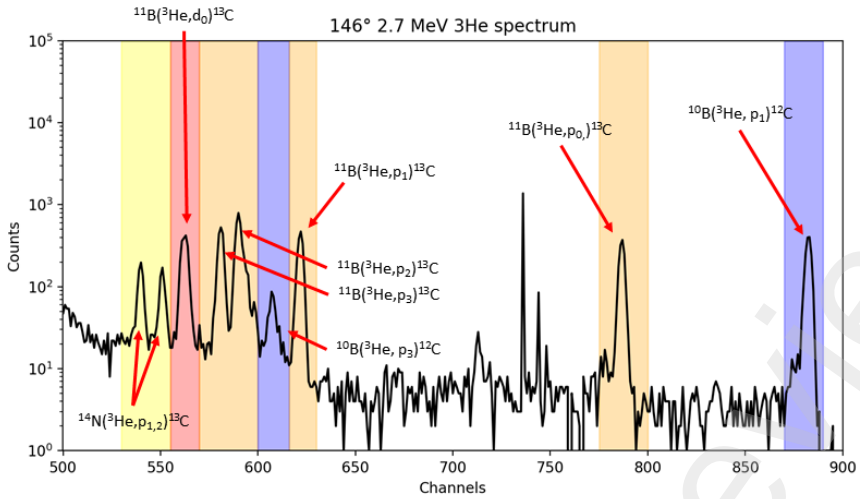

Figure 6 - Peak identification in the spectrum from fig. 4 b). Peaks of ^{14}N are also visible

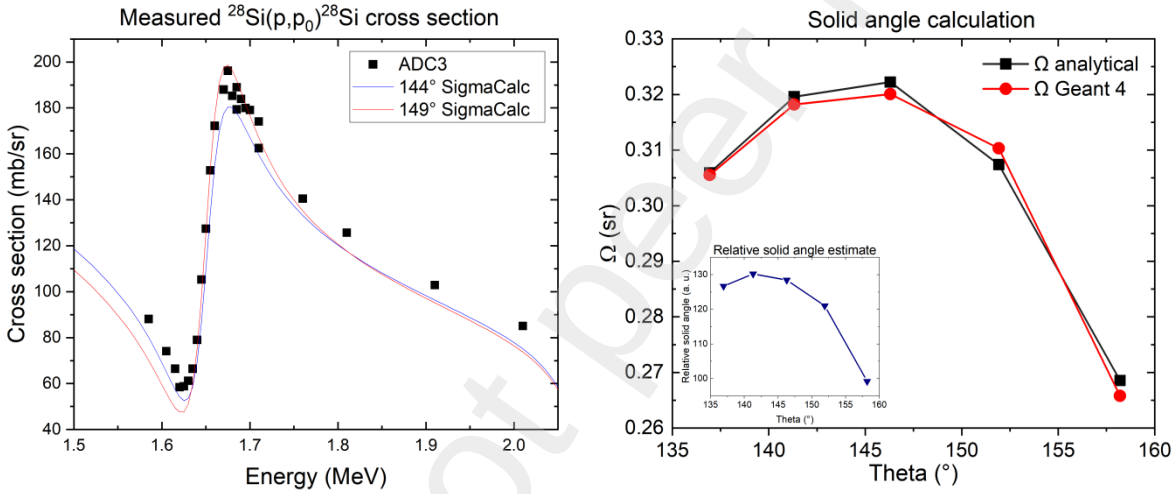

Figure 5 : Left - The $^{28}Si(p,p_0)^{28}Si$ data used for calibration. Right - Comparison of the values of the solid angle for different detector strips, inset is the relative calculation obtained from experiment

As an additional check we estimate the relative solid angle from the ^{3}He measurements using the Au Rutherford peaks. In each measurement Ω is proportional to $\frac{I_{Au}}{\sigma_{Au}}$. We then obtain the relative solid angle for each detector strip by averaging $\frac{I_{Au}}{\sigma_{Au}}$ over all of the energies collected. This is shown as an inset in Figure 5 and it appears to follow the trend of the calculated values.

3.1 Cross section results

The obtained results are given in Figure 7 for the two high Q-value reactions most relevant for NRA applications. A good agreement between the data obtained at 137° and those from McIntyre et al. [16] at 135° can be observed. The $^{10}B(^3He, p_1)^{12}C$ reaction shows significant angular dependence with a minimum at 141°, the cross sections vary from 0.3-0.8 mb/sr. On the contrary, $^{11}B(^3He, p_0)^{13}C$ reaction shows a smaller angular dependence, with the

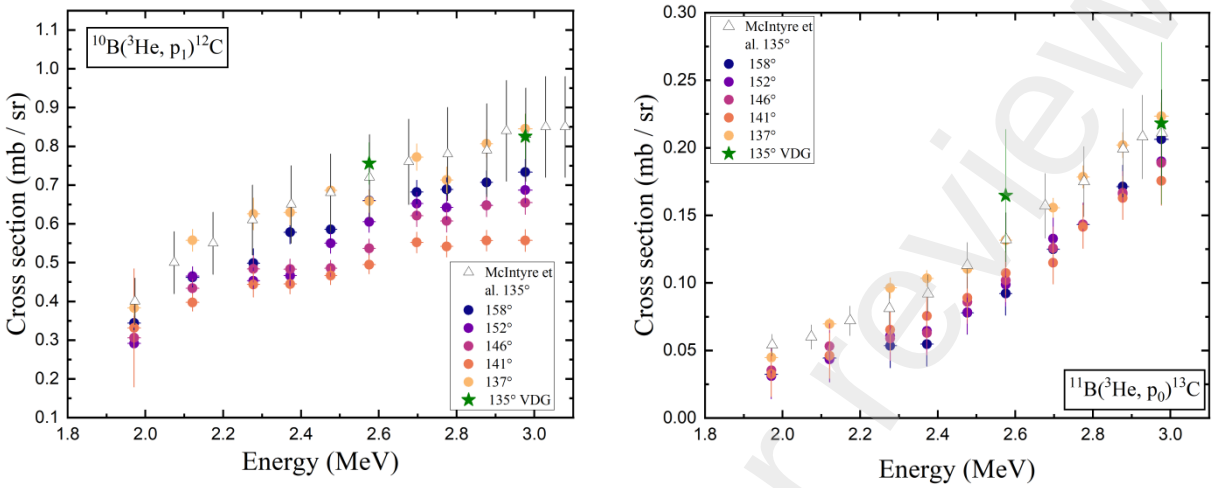

Figure 7 - Measured cross section values compared with those of McIntyre et al. (1996)

cross section sharply dropping after 137° and remaining flat afterwards while the cross sections are ten times smaller than the former reaction. For both reactions, the cross sections show an increase with respect to energy. As such, additional data at higher energies will be important for the NRA analysis of boron content in deeper layers of samples. The data reported concern the reactions $^{10}B(^3He, p_1)^{12}C$, $^{10}B(^3He, p_3)^{12}C$, $^{11}B(^3He, p_0)^{13}C$, $^{11}B(^3He, p_1)^{13}C$, $^{11}B(^3He, p_2)^{13}C$, $^{11}B(^3He, p_3)^{13}C$ and $^{11}B(^3He,d_0)^{12}C$.. The full dataset is given in the appendix and will be made available on the IBANDL database. Due to the kinematics there is an overlap between the $^{11}B(^3He, p_2)^{12}C$ and $^{14}N(^3He, p_2)^{16}O$ peaks in the spectrum and as such, some of the lower energy $^{11}B(^3He, p_2)^{13}C$ peaks were not able to be resolved. Therefore the $^{11}B(^3He, p_2)^{13}C$ reaction cross sections are reported for a smaller range of energies, depending on the reaction angle.

The benchmarking spectra obtained with a thick compressed boron target with measurements conducted both at RBI and at RUBION are shown in **Error! Reference source not found.** for the largest and smallest angle, along with the characterization of the target used for benchmarking. The $Qx\Omega$ value is obtained from the RBS cross section of gold and the known thickness of the gold layer on the top of the target (2.3 x 10^{15} at/cm^2). The simulated and experimental spectra agree within the available energy range (down to 2 MeV)

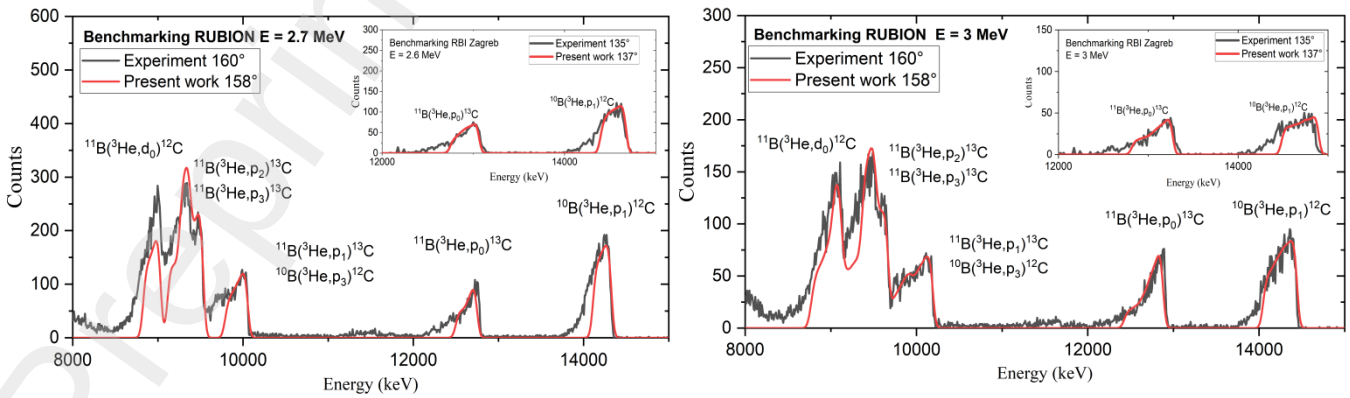

Figure 8 – Thick boron target benchmarking spectra (black line) obtained at RUBION Bochum and RBI Zagreb (inset). The red line indicates simulated spectra obtained with SIMNRA using the cross sections measured.

3.2 Uncertainties summary

The acceptance of each detector strip introduces an uncertainty in the calculation of the Rutherford cross section. The latter was estimated as half of the difference between the Rutherford cross section at the maximum and minimum geometrical angles of each strip as given in Figure 1.

$$\Delta\sigma_{Au}(\theta_1, \theta_2) = \frac{|\sigma_{Au}(\theta_2) - \sigma_{Au}(\theta_1)|}{2}$$

The relative uncertainty $\Delta\sigma_{Au}/\sigma_{Au}$ calculated in this way is independent of energy for a given strip and is between 2 and 3 percent. The uncertainty in the measurement of the ratio of thicknesses λ is calculated to be 2.6%, based on the uncertainties in the reaction cross sections from the literature and the obtained statistics. The uncertainty budget is summarized in Table 1.

Table 1 - Summary of the uncertainties of the parameters in the cross section as given in Equation 1 and the beam energy. The data shown is for nominal ^{3}He energy of 2.7 MeV and reaction angle 146°.

Parameter	Relative uncertainty (%)	Value	
Relative thickness		2.600	
Au RBS		2.754	
B Integral		2.317	
Au Integral		0.117	
Total B Cross section (mb/sr)		**4.687**	**0.81 ± 0.04**
Energy loss		0.26	
Magnetic calibration error		0.49	
Total Energy (keV)		**0.55**	**2698 ± 16**

The 90° analyzing magnet enables precise definition of the ion beam energy impinging on the target. Since the Si(p,p) reaction used to calibrate the angles (Figure 5) has a strong resonance in energy, this resonance was used to calibrate the magnetic field as well. The energy of the interaction was taken to be the average energy in the boron layer, this was calculated as $E = E_0 - \frac{\Delta E}{2}$ where E_0 is the impinging energy determined from the magnet calibration. The energy loss ΔE was calculated using SRIM, assuming bulk density of boron. The reported error in energy is given as the quadratic sum of this energy loss and the uncertainty in impinging energy from the magnetic calibration. All the relevant uncertainties are given in**Error! Reference source not found.** Table 1 for the example of the ^{10}B(^{3}He, p$_1$)^{12}C data at 146° and 2.7 MeV (Figure 6).

4 Conclusion

In the present work the differential cross-section data for the reactions ^{10}B(^{3}He, p$_1$)^{12}C, ^{10}B(^{3}He, p$_3$)^{12}C, ^{11}B(^{3}He, p$_0$)^{13}C, ^{11}B(^{3}He, p$_1$)^{13}C, ^{11}B(^{3}He, p$_2$)^{13}C, ^{11}B(^{3}He, p$_3$)^{13}C and ^{11}B(^{3}He,d$_0$)^{12}C was measured in the energy range 2 - 3 MeV and at backwards angles of 137°, 141°,146°, 152° and 158° using a new experimental setup developed for high yield µNRA studies. The large solid angle of the detector used, in parallel with precise angular definition, is especially useful in applications of ^{3}He-NRA, considering how time-consuming NRA measurements typically are with the relatively low currents that are available in microprobe setups. The obtained cross sections were benchmarked with a thick B target and fitted using SIMNRA. Compared to the literature, the 137° data agrees within error with the values of McIntyre et al. [16] for ^{11}B(^{3}He, p$_0$)^{13}C and McIntyre et al. and Patterson et al. [17] for ^{10}B(^{3}He,p$_1$)^{12}C. The data reported will be made available to the community on the IBANDL database for applications of ^{3}He-NRA in the analysis of boron containing materials.

Acknowledgments

The authors acknowledge the support from International Atomic Energy Agency through Coordinated Research project F11023 (IAEA Reasearch contract No. 24308), and from the European Union's Horizon 2020 Research and Innovation programme under Grant Agreement No 101004761.

5 References

[1] M. Mayer, S. Möller, M. Rubel, A. Widdowson, S. Charisopoulos, T. Ahlgren, E. Alves, G. Apostolopoulos, N. P. Barradas, S. Donnelly, S. Fazinić, K. Heinola, O. Kakuee, H. Khodja, A. Kimura, A. Lagoyannis, M. Li, S. Markelj, M. Mudrinic, P. Petersson, I. Portnykh, D. Primetzhofer, P. Reichart, D. Ridikas, T. Silva, S. M. Gonzalez de Vicente and Y. Q. Wang, "Ion beam analysis of fusion plasma-facing materials and components: facilities and research challenges," *Nuclear Fusion,* vol. 60, p. 025001, December 2019.

[2] S. Fazinić, I. Božičević-Mihali, G. Provatas, T. Tadić, M. Rubel, E. Fortuna-Zaleśna and A. Widdowson, "Micro-analyses of dust particles generated in the JET tokamak with the ITER-like wall," *Nuclear Fusion,* vol. 60, p. 126031, October 2020.

[3] ITER organization, " ITER Baseline | STAC committee reviews new plans for construction and operation," October 2023. [Online]. Available: https://www.iter.org/newsline/-/3935.

[4] G. Provatas, S. Fazinić, N. Soić, N. Vukman, D. Cosic, M. Krmpotić, M. Vukšić, A. Crnjac, R. Popočovski, L. Palada, P. Čolović, D. Dell'Aquila, I. Gašparić, D. J. Malenica, T. Mijatović and M. Uroić, "Differential cross section measurements of the 9Be(3He,p)11B reaction for NRA applications," *Nuclear Instruments and Methods in Physics Research Section B: Beam Interactions with Materials and Atoms,* vol. 472, p. 36–45, June 2020.

[5] G. Provatas, S. Fazinić, N. Soić, N. Vukman, D. Cosic, M. Krmpotić, L. Palada, R. Popočovski, D. Dell'Aquila, M. Jakšić, M. Kokkoris and F. Maragkos, "Systematic study of the Systematic study of the ^{12}C (^{3}He, p) ^{14}N reaction for NRA applications" *Nuclear Instruments and Methods in Physics Research Section B: Beam Interactions with Materials and Atoms,* vol. 500–501, p. 57–67, August 2021.

[6] S. Fazinić, T. Tadić, M. Vukšić, M. Rubel, P. Petersson, E. Fortuna-Zaleśna and A. Widdowson, "Ion Microbeam Analyses of Dust Particles and Codeposits from JET with the ITER-Like Wall," *Analytical Chemistry,* vol. 90, p. 5744–5752, April 2018.

[7] "Micron Semiconductors," [Online]. Available: https://www.micronsemiconductor.co.uk/.

[8] M. Jakšić, G. Provatas, I. B. Mihalić, A. Crnjac, D. Cosic, T. Dunatov, O. Romanenko and Z. Siketić, "The dual ion beam microprobe," *Nuclear Instruments and Methods in Physics Research Section B: Beam Interactions with Materials and Atoms,* vol. 539, p. 120–126, June 2023.

[9] R. Salomonovicˇ, "Angular distribution of proton non-Rutherford elastic scattering cross section of carbon and silicon," *Nuclear Instruments and Methods in Physics Research Section B: Beam Interactions with Materials and Atoms,* vol. 82, p. 1–6, July 1993.

[10] M. Jakšić, I. Bogdanović Radović, M. Bogovac, V. Desnica, S. Fazinić, M. Karlušić, Z. Medunić, H. Muto, Ž. Pastuović, Z. Siketić, N. Skukan and T. Tadić, "New capabilities of the Zagreb ion microbeam system," *Nuclear Instruments and Methods in Physics Research Section B: Beam Interactions with Materials and Atoms,* vol. 260, p. 114–118, July 2007.

[11] M. Mayer, "SIMNRA user's guide.," 1997.

[12] M. Kokkoris, A. Kafkarkou, V. Paneta, R. Vlastou, P. Misaelides and A. Lagoyannis, "Differential cross sections for the 11B(p,αo)8Be and 11B(p,p0)11B reactions, suitable for ion beam analysis," *Nuclear Instruments and Methods in Physics Research Section B: Beam Interactions with Materials and Atoms,* vol. 268, p. 3539–3545, December 2010.

[13] M. Chiari, L. Giuntini, P. A. Mandò and N. Taccetti, "Proton elastic scattering cross-section on boron from 0.5 to 3.3 MeV," *Nuclear Instruments and Methods in Physics Research Section B: Beam Interactions with Materials and Atoms,* vol. 184, p. 309–318, November 2001.

[14] V. Foteinou, F. Maragkos, H.-W. Becker, L. Hess, K. Ivanković, M. Kokkoris, M. Mayer, G. Provatas and D. Rogalla, "Differential cross-section measurements for the 9Be(3He,3He0)9Be elastic scattering and the 9Be(3He,px)11B reactions," *Nuclear Instruments and Methods in Physics Research Section B: Beam Interactions with Materials and Atoms,* vol. 542, p. 158–175, September 2023.

[15] F. A, "Tv User-Manual," 2000.

[16] L. C. McIntyre, J. A. Leavitt, M. D. Ashbaugh, J. Borgardt, E. Andrade, J. Rickards and A. Oliver, "Cross section measurements for the (3He, p) nuclear reaction on B and N between 2 and 4 MeV," *Nuclear Instruments and Methods in Physics Research Section B: Beam Interactions with Materials and Atoms,* vol. 118, p. 219–223, September 1996.

[17] J. R. Patterson, J. M. Poate and E. W. Titterton, "States of 13N in the 20-30 MeV region," *Proceedings of the Physical Society,* vol. 88, p. 641–648, July 1966.

[18] J. P. Schiffer, T. W. Bonner, R. H. Davis and F. W. Prosser, "Study of the Reaction Mechanism for Study of the Reaction Mechanism for (^{3}He, p) Reactions with ^{6}Li, ^{10}B, and ^{13}C" *Physical Review,* vol. 104, p. 1064–1068, November 1956.

Appendix – all data obtained:

137°

Energy (MeV)	Uncertainty (MeV)	^{10}B(^{3}He,p$_1$)^{12}C Cross section (mb/sr)	Uncertainty (mb/sr)	^{11}B(^{3}He,p$_0$)^{13}C Cross section (mb/sr)	Uncertainty (mb/sr)	^{11}B(^{3}He,p$_1$)^{12}C Cross section (mb/sr)	Uncertainty (mb/sr)
2.976	0.018	0.846	0.039	0.223	0.01	0.198	0.009
2.877	0.016	0.807	0.035	0.202	0.009	0.195	0.009
2.775	0.016	0.728	0.034	0.178	0.008	0.178	0.008
2.698	0.016	0.760	0.034	0.156	0.007	0.165	0.008
2.575	0.016	0.658	0.029	0.132	0.006	0.15	0.007
2.476	0.016	0.685	0.032	0.11	0.005	0.132	0.006
2.372	0.016	0.630	0.032	0.103	0.006	0.108	0.006
2.278	0.016	0.623	0.041	0.096	0.008	0.105	0.008
2.121	0.017	0.558	0.028	0.07	0.004	0.074	0.005
1.971	0.017	0.383	0.019	0.045	0.003	0.053	0.003

Energy (MeV)	Uncertainty (MeV)	^{11}B(^{3}He,p$_3$)^{13}C Cross section (mb/sr)	Uncertainty (mb/sr)	^{11}B(^{3}He,d$_0$)^{12}C Cross section (mb/sr)	Uncertainty (mb/sr)
2.976	0.018	0.180	0.009	0.178	0.009
2.877	0.016	0.192	0.009	0.173	0.008
2.775	0.016	0.184	0.009	0.178	0.009
2.698	0.016	0.198	0.009	0.174	0.008
2.575	0.016	0.183	0.008	0.163	0.007
2.476	0.016	0.173	0.008	0.146	0.007
2.372	0.016	0.163	0.008	0.147	0.008
2.278	0.016	0.171	0.011	0.105	0.009
2.121	0.017	0.149	0.008	0.090	0.005
1.971	0.017	0.115	0.006	0.067	0.004

Energy (MeV)	Uncertainty (MeV)	$^{10}B(^{3}He,p_3)^{12}C$ Cross section (mb/sr)	Uncertainty (mb/sr)
2.976	0.018	0.111	0.011
2.877	0.016	0.121	0.009
2.775	0.016	0.122	0.011
2.698	0.016	0.120	0.009
2.575	0.016	0.112	0.008
2.476	0.016	0.091	0.008
2.372	0.016	0.092	0.010
2.278	0.016	0.092	0.014
2.121	0.017	0.079	0.009
1.971	0.017	0.058	0.006

141°

Energy (MeV)	Uncertainty (MeV)	$^{10}B(^{3}He,p_1)^{12}C$ Cross section (mb/sr)	Uncertainty (mb/sr)	$^{11}B(^{3}He,p_0)^{13}C$ Cross section (mb/sr)	Uncertainty (mb/sr)	$^{11}B(^{3}He,p_1)^{12}C$ Cross section (mb/sr)	Uncertainty (mb/sr)
2.976	0.018	0.558	0.028	0.177	0.009	0.304	0.014
2.877	0.016	0.557	0.027	0.179	0.008	0.306	0.013
2.775	0.016	0.542	0.027	0.164	0.008	0.279	0.013
2.698	0.016	0.544	0.026	0.153	0.007	0.285	0.013
2.575	0.016	0.495	0.024	0.127	0.006	0.245	0.011
2.476	0.016	0.466	0.023	0.118	0.006	0.227	0.011
2.372	0.016	0.445	0.025	0.104	0.006	0.211	0.011
2.278	0.016	0.442	0.033	0.084	0.007	0.186	0.012
2.121	0.017	0.397	0.022	0.072	0.004	0.154	0.008
1.971	0.017	0.270	0.015	0.048	0.003	0.099	0.005

Energy (MeV)	Uncertainty (MeV)	$^{11}B(^{3}He,p_2)^{12}C$ Cross section (mb/sr)	Uncertainty (mb/sr)	$^{11}B(^{3}He,p_3)^{13}C$ Cross section (mb/sr)	Uncertainty (mb/sr)	$^{11}B(^{3}He,d_0)^{12}C$ Cross section (mb/sr)	Uncertainty (mb/sr)
2.976	0.018	0.281	0.013	0.186	0.009	0.175	0.009
2.877	0.016	0.273	0.012	0.187	0.009	0.177	0.008
2.775	0.016	0.247	0.013	0.174	0.009	0.16	0.008
2.698	0.016	0.282	0.013	0.172	0.008	0.172	0.008
				0.16	0.008	0.172	0.008
				0.145	0.007	0.136	0.007
				0.158	0.009	0.151	0.008
				0.139	0.010	0.126	0.009
				0.138	0.007	0.104	0.006
				0.117	0.006	0.061	0.004

Energy (MeV)	Uncertainty (MeV)	$^{10}B(^{3}He,p_3)^{12}C$ Cross section (mb/sr)	Uncertainty (mb/sr)
2.976	0.018	0.142	0.011
2.877	0.016	0.112	0.009
2.775	0.016	0.094	0.009
2.698	0.016	0.103	0.009

2.575	0.016	0.09	0.008
2.476	0.016	0.086	0.008
2.372	0.016	0.087	0.01
2.278	0.016	0.088	0.015
2.121	0.017	0.084	0.009
1.971	0.017	0.044	0.005

146°

Energy (MeV)	Uncertainty (MeV)	$^{10}B(^{3}He,p_1)^{12}C$ Cross section (mb/sr)	Uncertainty (mb/sr)	$^{11}B(^{3}He,p_0)^{13}C$ Cross section (mb/sr)	Uncertainty (mb/sr)	$^{11}B(^{3}He,p_1)^{12}C$ Cross section (mb/sr)	Uncertainty (mb/sr)
2.976	0.018	0.655	0.031	0.189	0.009	0.181	0.008
2.877	0.016	0.648	0.029	0.167	0.007	0.171	0.008
2.775	0.016	0.608	0.029	0.143	0.007	0.172	0.008
2.698	0.016	0.612	0.028	0.126	0.006	0.160	0.007
2.575	0.016	0.537	0.024	0.102	0.005	0.140	0.006
2.476	0.016	0.485	0.021	0.086	0.004	0.122	0.006
2.372	0.016	0.484	0.026	0.063	0.004	0.105	0.006
2.278	0.016	0.482	0.034	0.059	0.006	0.096	0.007
2.121	0.017	0.434	0.023	0.053	0.003	0.063	0.004
1.971	0.017	0.306	0.016	0.035	0.002	0.053	0.003

Energy (MeV)	Uncertainty (MeV)	$^{11}B(^{3}He,p_2)^{12}C$ Cross section (mb/sr)	Uncertainty (mb/sr)	$^{11}B(^{3}He,p_3)^{13}C$ Cross section (mb/sr)	Uncertainty (mb/sr)	$^{11}B(^{3}He,d_0)^{12}C$ Cross section (mb/sr)	Uncertainty (mb/sr)
2.976	0.018	0.287	0.013	0.194	0.009	0.189	0.009
2.877	0.016	0.278	0.012	0.200	0.009	0.185	0.008
2.775	0.016	0.273	0.013	0.187	0.009	0.178	0.008
2.698	0.016	0.260	0.012	0.183	0.008	0.174	0.008
				0.182	0.008	0.157	0.007
				0.162	0.007	0.153	0.007
				0.143	0.007	0.129	0.007
				0.150	0.010	0.116	0.008
				0.128	0.007	0.094	0.005
				0.119	0.006	0.066	0.004

Energy (MeV)	Uncertainty (MeV)	$^{10}B(^{3}He,p_3)^{12}C$ Cross section (mb/sr)	Uncertainty (mb/sr)
2.976	0.018	0.141	0.011
2.877	0.016	0.123	0.009
2.775	0.016	0.115	0.009
2.698	0.016	0.114	0.009
2.575	0.016	0.094	0.007
2.476	0.016	0.090	0.008
2.372	0.016	0.089	0.009
2.278	0.016	0.099	0.015
2.121	0.017	0.071	0.008
1.971	0.017	0.064	0.006

152°

Energy (MeV)	Uncertainty (MeV)	$^{10}B(^{3}He,p_1)^{12}C$ Cross section (mb/sr)	Uncertainty (mb/sr)	$^{11}B(^{3}He,p_0)^{13}C$ Cross section (mb/sr)	Uncertainty (mb/sr)	$^{11}B(^{3}He,p_1)^{12}C$ Cross section (mb/sr)	Uncertainty (mb/sr)
2.976	0.018	0.687	0.033	0.190	0.010	0.177	0.008
2.877	0.016	0.648	0.029	0.166	0.007	0.178	0.008
2.775	0.016	0.642	0.031	0.143	0.007	0.161	0.008
2.698	0.016	0.652	0.029	0.133	0.006	0.167	0.008
2.575	0.016	0.605	0.027	0.099	0.005	0.146	0.007
2.476	0.016	0.55	0.026	0.078	0.004	0.125	0.006
2.372	0.016	0.466	0.026	0.064	0.004	0.098	0.006
2.278	0.016	0.453	0.033	0.061	0.006	0.091	0.008
2.121	0.017	0.465	0.024	0.043	0.003	0.07	0.004
1.971	0.017	0.687	0.018	0.031	0.002	0.048	0.003

Energy (MeV)	Uncertainty (MeV)	$^{11}B(^{3}He,p_2)^{12}C$ Cross section (mb/sr)	Uncertainty (mb/sr)	$^{11}B(^{3}He,p_3)^{13}C$ Cross section (mb/sr)	Uncertainty (mb/sr)	$^{11}B(^{3}He,d_0)^{12}C$ Cross section (mb/sr)	Uncertainty (mb/sr)
2.976	0.018	0.299	0.013	0.197	0.009	0.190	0.009
2.877	0.016	0.273	0.012	0.193	0.008	0.178	0.008
2.775	0.016	0.269	0.013	0.187	0.009	0.172	0.008
2.698	0.016	0.268	0.012	0.19	0.008	0.18	0.008
2.575	0.016	0.257	0.011	0.186	0.008	0.169	0.008
2.476	0.016	0.244	0.011	0.17	0.008	0.144	0.007
2.372	0.016	0.204	0.010	0.155	0.008	0.137	0.007
				0.147	0.01	0.124	0.009
				0.14	0.007	0.085	0.005
				0.125	0.006	0.066	0.004

Energy (MeV)	Uncertainty (MeV)	$^{10}B(^{3}He,p_3)^{12}C$ Cross section (mb/sr)	Uncertainty (mb/sr)
2.976	0.018	0.144	0.012
2.877	0.016	0.127	0.009
2.775	0.016	0.116	0.01
2.698	0.016	0.121	0.009
2.575	0.016	0.100	0.008
2.476	0.016	0.103	0.008
2.372	0.016	0.081	0.009
2.278	0.016	0.087	0.014
2.121	0.017	0.083	0.008
1.971	0.017	0.071	0.007

158°

Energy (MeV)	Uncertainty (MeV)	$^{10}B(^{3}He,p_1)^{12}C$ Cross section (mb/sr)	Uncertainty (mb/sr)	$^{11}B(^{3}He,p_0)^{13}C$ Cross section (mb/sr)	Uncertainty (mb/sr)	$^{11}B(^{3}He,p_1)^{12}C$ Cross section (mb/sr)	Uncertainty (mb/sr)
2.976	0.018	0.734	0.034	0.206	0.009	0.173	0.008

2.877	0.016	0.707	0.03	0.171	0.008	0.18	0.008
2.775	0.016	0.69	0.032	0.143	0.007	0.172	0.008
2.698	0.016	0.672	0.03	0.125	0.006	0.151	0.007
2.575	0.016	0.66	0.028	0.092	0.005	0.137	0.006
2.476	0.016	0.585	0.027	0.078	0.004	0.12	0.006
2.372	0.016	0.579	0.03	0.055	0.004	0.104	0.006
2.278	0.016	0.497	0.037	0.054	0.006	0.092	0.008
2.121	0.017	0.462	0.024	0.044	0.004	0.062	0.004
1.971	0.017	0.344	0.018	0.032	0.002	0.055	0.003

Energy (MeV)	Uncertainty (MeV)	$^{11}B(^{3}He,p_2)^{12}C$ Cross section (mb/sr)	Uncertainty (mb/sr)	$^{11}B(^{3}He,p_3)^{13}C$ Cross section (mb/sr)	Uncertainty (mb/sr)	$^{11}B(^{3}He,d_0)^{12}C$ Cross section (mb/sr)	Uncertainty (mb/sr)
2.976	0.018	0.276	0.012	0.206	0.009	0.188	0.015
2.877	0.016	0.276	0.011	0.203	0.009	0.182	0.008
2.775	0.016	0.279	0.012	0.199	0.009	0.196	0.009
2.698	0.016	0.272	0.011	0.2	0.009	0.181	0.008
2.575	0.016	0.260	0.011	0.177	0.008	0.169	0.007
2.476	0.016	0.226	0.010	0.176	0.008	0.148	0.007
2.372	0.016	0.188	0.010	0.152	0.008	0.129	0.007
				0.161	0.011	0.124	0.01
				0.148	0.008	0.097	0.006
				0.137	0.006	0.014	0.002

Energy (MeV)	Uncertainty (MeV)	$^{10}B(^{3}He,p_3)^{12}C$ Cross section (mb/sr)	Uncertainty (mb/sr)
2.976	0.018	0.122	0.012
2.877	0.016	0.131	0.01
2.775	0.016	0.107	0.011
2.698	0.016	0.13	0.011
2.575	0.016	0.091	0.008
2.476	0.016	0.09	0.009
2.372	0.016	0.068	0.009
2.278	0.016	0.036	0.012
2.121	0.017	0.069	0.009
1.971	0.017	0.261	0.016